Journal of Materials Chemistry C

PAPER

Check for updates

Direct and continuous hydrothermal flow synthesis of thermochromic phase pure monoclinic VO₂ nanoparticles†

Delphine Malarde, [ID] ‡[a] Ian D. Johnson, [ID] ‡[a] Ian J. Godfrey, [ID] [a]
Michael J. Powell, [ID] [a] Giannantonio Cibin, [ID] [b] Raul Quesada-Cabrera,[a]
Jawwad A. Darr, [ID] [a] Claire J. Carmalt, [ID] [a] Gopinathan Sankar,[a] Ivan P. Parkin [ID] [a]
and Robert G. Palgrave [ID] *[a]

Monoclinic vanadium(IV) oxide [VO₂(M)] is a widely studied material due to its thermochromic properties and its potential use in energy-efficient glazing applications. VO₂(M) nanoparticles can be a great advantage for energy-efficient glazing as below 50 nm the nanoparticles poorly interact with visible wavelengths – resulting in an increase in visible light transmittance whilst maintaining the thermochromic response of the material. The direct synthesis of VO₂(M) nanoparticles with effective thermochromic properties will be a step forward towards industrial applications of this material. Unfortunately, many of the synthesis processes reported so far involve multiple steps, including post-treatment, and the synthesis is not always reproducible. In this study, we present the first direct synthesis of pure monoclinic VO₂ nanoparticles by continuous hydrothermal flow synthesis (CHFS). TEM images showed that nanoparticles in the size range of 30–40 nm were produced. The VO₂(M) nanoparticles also showed good thermochromic properties with a solar modulation (ΔT_{sol}) of 3.8%, as established by UV/Vis spectroscopy. A range of analytical methods was used to characterise the materials, including X-ray absorption spectroscopy (XANES and EXAFS), X-ray diffraction (XRD), X-ray photoelectron spectroscopy (XPS) and transmission electron microscopy (TEM). The influence of niobium (Nb) doping on the physical and thermochromic properties of the VO₂ nanoparticles was also explored. Previous work has shown a sharp metal-to-semiconductor transition of VO₂ upon incorporation of a Nb dopant. The results of the current work suggested that these changes are likely due to changes on the local structure of the oxide.

Introduction

The numerous crystal structures and phase transitions of vanadium(IV) oxide (VO₂) make it a promising material for a wide range of applications including batteries,[1,2] gas sensors[3] and solar control coatings for smart windows.[4,5] The monoclinic form of vanadium dioxide, VO₂(M) (space group $P121/c1$) has attracted great interest due to its thermochromic properties. VO₂(M) has the ability to reversibly transform from the semiconducting monoclinic phase VO₂(M) to the semi-metallic rutile phase VO₂(R) (space group $P42/mnm$).[6] The reversible metal-to-semiconductor transition (MST) occurs at *ca.* 68 °C for

a typical undoped VO₂ material.[7] When heated beyond this temperature, the material's optical properties change drastically – from highly transmissive to highly reflective – in the NIR region, and its electrical conductivity increases by several orders of magnitude.[8] The thermochromic properties of VO₂(M) and its relatively low temperature transition, *i.e.* close to room temperature, make it an interesting material for energy-efficient glazing applications.

The strong absorption of VO₂(M), however, as well as its high reflectivity due to its narrow band gap has a negative impact on both visible light transmittance (T_{lum}) and solar modulation (ΔT_{sol}) – two essential parameters for measuring the energy saving efficiency of glazing. T_{lum} indicates the percentage of visible light passing through the coated glass while ΔT_{sol} represents the ability of the coating to modulate the solar energy. It had been quite challenging to optimize both parameters as the increase of T_{lum} often induces a reduction of ΔT_{sol}, and *vice versa*.

Li *et al.*[9,10] showed that both parameters T_{lum} and ΔT_{sol} could be significantly improved simultaneously by embedding

[a] *Department of Chemistry, Materials Chemistry Centre, University College London, 20 Gordon Street, London WC1H 0AJ, UK. E-mail: r.palgrave@ucl.ac.uk*

[b] *Diamond Light Source Ltd, Diamond House Harwell Science and Innovation Campus Didcot, Oxfordshire OX11 0DE, UK*

† Electronic supplementary information (ESI) available. See DOI: 10.1039/c8tc00859k

‡ These authors contributed equally.

VO_2 nanoparticles in a host material rather than synthesising a continuous VO_2 film. It has been established, for example, that a 5 μm thick film of 1 vol% of well-dispersed VO_2 nanoparticles shows higher T_{lum} and ΔT_{sol} values compared to an equivalent continuous VO_2 film with a thickness of 50 nm.[11] In addition, it has been demonstrated that VO_2 nanoparticles of *ca.* 50 nm (or less) weakly interact with visible light while those with particle sizes of *ca.* 20 nm or less suppress optical scattering.[4,12] Hence, it is important to tailor particle sizes and dispersion thereof.

The direct synthesis of $VO_2(M)$ nanoparticles can be challenging due to the multiple valence states of the vanadium ion and the ease of oxidation/reduction of V^{4+} to V^{5+}/V^{3+} species. The synthesis of phase pure monoclinic VO_2 can require several steps including post-synthesis heat-treatment. Any additional processing of the material risks oxidation or reduction of the vanadium, reducing or destroying the functionality. Hydrothermal synthesis is a common route to obtain $VO_2(M)$ nanoparticles, however, this method typically requires 24 to 48 hours to produce phase pure $VO_2(M)$ nanoparticles in a batch process and it is hardly reproducible.[13,14]

Continuous hydrothermal flow synthesis (CHFS) is a method used to produce nanoparticles. CHFS has the advantage of being a direct, reproducible and scalable method.[15] Unlike batch hydrothermal processes, CHFS is a continuous process, thus once a system is optimised it is possible to produce kg of material per hour. In CHFS, a stream of supercritical water is mixed with an ambient temperature stream of metal precursor salts (in an engineered mixer) to almost instantly form nanoparticles in a good yield (typically above 85%). In this process, metal oxide nanoparticles are produced very rapidly by the hydrolysis and subsequent dehydration (or degradation) of the metal salts.[16,17] Previously, CHFS has been utilised to prepare $VO_2(M)$ and Nb-doped $VO_2(M)$ samples in a two-step process, where the initial VO_2 product contained impurities and required post-synthesis annealing at 600 °C to obtain phase pure $VO_2(M)$.[1,18,19] This was synthesised at a reaction mixing temperature of 335 °C using balanced flow rates for the sc-water and ambient temperature metal salt feed. However, to the authors' knowledge, there are no reports on the successful direct synthesis of pure $VO_2(M)$ using a continuous method.

In this study, we present the first direct continuous hydrothermal flow synthesis of $VO_2(M)$ nanoparticles, which has been achieved by the modification of the CHFS apparatus and under unbalanced flow rate conditions. A vanadium(IV) precursor solution, obtained from the reduction of vanadium(V) oxide (V_2O_5) by oxalic acid ($H_2C_2O_4$), was used for the synthesis of the nanoparticles. The phase purity and the characteristics of the nanoparticles were investigated by X-ray absorption spectroscopy (XANES and EXAFS), X-ray diffraction, X-ray photoelectron spectroscopy and transmission electron microscopy. The thermochromic properties of the as-formed nanoparticles were determined by variable temperature UV-Vis spectroscopy. This study presents a key step towards the industrial applications of thermochromic VO_2 materials.

Experimental

All chemical compounds used in the synthesis were purchased from Sigma-Aldrich.

Synthesis of the precursor solution

An aqueous V^{5+}-containing solution (5 L) was prepared from a mixture of 181.88 g of V_2O_5 and 360.12 g oxalic acid in D.I. water (vanadium : oxalic acid, 1 : 4 ratio). This solution (0.4 M) was stirred for 48 h until it was fully reduced, as evidenced by a colour change to a blue V^{4+}-containing solution. This initial solution was diluted to 0.2 M and used directly in the CHFS process as a precursor solution.

Continuous hydrothermal flow synthesis (CHFS) of VO_2 nanoparticles

$VO_2(M)$ was synthesised using a lab-scale CHFS process, which was modified from previous reports to achieve higher mixing-point temperatures.[20] This required 80 mL min^{-1} of 450 °C D.I. water and 10 mL min^{-1} combined precursor feeds to obtain a theoretical mixing point temperature of *ca.* 402 °C.[18] The hot water feed was provided by a Primeroyal K pump (Milton Roy, Pont Saint-Pierre, France), and the precursors were provided by two Gilson-type pumps (Gilson 305, Fig. 1, pumps G1 and G2) operating at flow rates of 5 mL min^{-1} each. The flow rates were controlled using the actuators on the pumps, which were calibrated using the LabView software (LabView, National Instruments, Berkshire, UK). Both pumps G1 and G2 provided the V^{4+} precursor detailed in the previous paragraph. The outputs of the pumps were connected to pressure gauges (EN 837-1, WIKA Instruments Ltd, Redhill, UK), and pressure relief valves (R3A series, Swagelok) set to a relief pressure of 276 bar, a lift check valve (50 Series, Swagelok) and a non-return valve (CH Series, Swagelok) in series. The outputs of the Gilson pumps combined in a 1/8″ tee-piece, which subsequently flowed into a 4-way switch valve. This switch valve was also connected to the fourth pump (P4 Milton Roy Primeroyal K pump), an exhaust pipe with a Tescom BPR and the mixing point in the reactor. The 4-way valve (7921F4Y, LAA UK Ltd, Middlesex, UK) enabled the Gilson pumps to be pressurized and depressurized in isolation from the reactor, *i.e.* pump P4 and the Gilson pumps could be interchanged using the valve.

During synthesis, G1 and G2 were both employed to feed the 0.2 M V^{4+} precursor solution into the reactor. The combined output of G1 and G2 flowed into a Confined Jet Mixer (CJM), where it combined with the hot water feed from P1.[21] The theoretical mixing temperature was 402 °C for all reactions. The Reynolds number of the combined feed was *ca.* 14 000 and 22 000 for the 1/8″ and 1/16″ inlet pipe reactor configurations, namely configurations A and B, respectively. Configuration A was employed to synthesise the pure VO_2 sample while configuration B was used to synthesise the Nb-doped VO_2 sample. In both cases, the extremely high Reynolds numbers resulted in very rapid and turbulent mixing between the hot water feed and the precursors. Thus, the CJM allowed complete mixing within 50 ms of combination,[21] which occurred just beyond the supercritical
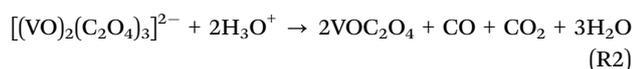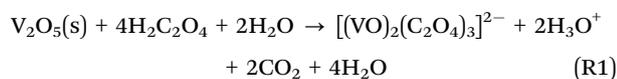
11732 | *J. Mater. Chem. C,* 2018, **6**, 11731–11739

This journal is © The Royal Society of Chemistry 2018

Fig. 1 Schematic diagram of the continuous hydrothermal flow synthesis (CHFS) process used in the direct synthesis of VO$_2$(M) nanoparticles.

water inlet pipe within the cross-piece as indicated in Fig. S1 (ESI†). The extremely high Reynolds number resulted in very rapid and turbulent mixing between the hot water feed and the precursors, which therefore caused rapid nucleation of the VO$_2$ product within the 1/4″ outlet pipe of the CJM (Fig. S1, ESI†). As the temperature of the combined feeds was 402 °C, the water solvent was still in the supercritical state. The output slurry flowed through a 1.4 m section of the 1/4″ pipe, giving a residence time of 1.0 s, before flowing through a pipe-in-pipe counter-current cooling section to reduce the slurry temperature to *ca.* 40 °C. The cooled product slurry exited the apparatus *via* a back-pressure regulator (Tescom, model 26-1762-24-194, Emerson Process Management Regulator Technologies Inc., South Lanarkshire, UK), which maintained a pressure of 240 bar in the system.

After synthesis, the supernatant was decanted from the product slurry and the concentrated paste was centrifuged at 4500 rpm for 5 minutes. The centrifuged sludge was repeatedly resuspended in D.I. water and centrifuged until the conductivity of the supernatant was reduced below 100 μS m^{-1}. The cleaned, wet product was placed in a freeze-drier (Virtis Genesis 35XL) and slowly heated from −60 °C to 25 °C, over 24 h under a vacuum of <13 Pa.

Film analysis

X-Ray Diffraction (XRD) was performed using a Stoe StadiP diffractometer in the transmission mode (coupled θ–2θ geometry),

with the sample sandwiched between two plastic foil disks held together with a thin layer of silicone grease. A pre-sample Ge(111) monochromator selected Mo-K$_{\alpha 1}$ radiation only (λ = 0.709 Å) and included a 0.5 mm collimator restricted to 3 mm height. The sample was rotated in the beam, and the diffraction intensity was recorded using a Dectris Mythen 1k silicon strip detector covering 18° (2θ). XRD patterns were collected in the 2θ range of 2° to 40° with a step size of 0.02° in 2θ and were compared to the ICSD reference pattern for monoclinic VO$_2$ (ICSD 34033).

The surface morphologies of the films were determined by Scanning Electron Microscopy (SEM) using a JEOL JSM-6700 (3 kV).

X-ray photoelectron spectroscopy (XPS) was carried out on powder using a Thermo Scientific K-alpha spectrometer with monochromated Al K$_\alpha$ radiation, a dual beam charge compensation system and at a constant pass energy of 50 eV (spot size 400 μm). Spectra were recorded from 0 to 1200 eV.

Transmission electron microscopy (TEM) images were obtained using a TEM Jeol 2100 with a LaB$_6$ source operating at an acceleration voltage of 200 kV.

The optical transmittances were monitored using a Perkin Elmer Lambda 950 UV-Vis-NIR spectrophotometer that was equipped with a homemade heating unit. The powder was deposited onto a silica barrier (50 nm SiO$_2$ layer) float glass, supplied by Pilkington/NSG. The thermochromic properties of the deposited films were measured by recording their transmittance spectra from 2500 nm to 250 nm at two different temperatures (20 °C and 90 °C).

To investigate the local structure of the samples, V K-edge X-ray absorption spectra were recorded on beamline B18 at diamond light source.[22] B18 was equipped with a Si(111) dual-crystal monochromator and Pt-coated harmonic rejection mirrors. The samples were pressed into pellets, with cellulose added as the binding agent, and data were recorded in transmission mode; data for a V foil reference were recorded simultaneously with each sample. Commercial monoclinic vanadium dioxide was obtained from Sigma Aldrich and measured as a standard compound. Multiple spectra of each sample were averaged prior to data analysis. Data reduction and fitting were carried out using the Demeter 0.9.25 suite of programmes.[23] Data fitting was performed in R-space.

Results and discussion

Continuous hydrothermal flow synthesis and characterisation

Continuous hydrothermal flow synthesis (CHFS) was used to produce VO_2(M) nanoparticles in a single step as a black powder suspension, which was cleaned and freeze-dried to yield a black powder. The vanadium(IV) precursor solution used for the synthesis was obtained from the reduction of vanadium(V) oxide by oxalic acid according to the accepted decomposition pathway shown in eqn (R1)–(R3)[18,24,25]

$$V_2O_5(s) + 4H_2C_2O_4 + 2H_2O \rightarrow [(VO)_2(C_2O_4)_3]^{2-} + 2H_3O^+ $$
$$+ 2CO_2 + 4H_2O \quad \text{(R1)}$$

$$[(VO)_2(C_2O_4)_3]^{2-} + 2H_3O^+ \rightarrow 2VOC_2O_4 + CO + CO_2 + 3H_2O$$
$$\text{(R2)}$$

$$2VOC_2O_4 \rightarrow VO_2 + CO + CO_2 \quad \text{(R3)}$$

The X-ray diffraction (XRD) patterns of the undoped and Nb-doped samples both matched the VO_2(M) reference exclusively (PDF Card No. 01-076-0456) (Fig. 2). An additional broad feature observed in these patterns at $2\theta \sim 5°$ was due to the silicone-based matrix used during the sample preparation.[26] This is in direct contrast to previous CHFS works, which resulted in a mixture of VO_2 phases and required heat treatment to 600 °C to produce the phase-pure VO_2(M).[18] It is suggested that the higher reaction temperature (*ca.* 402 °C compared to 335 °C) employed herein was necessary to drive complete conversion to the VO_2(M) phase in flow. The ability to manufacture VO_2(M) directly in a continuous process has no precedent, as the majority of synthesis methods are batch hydrothermal, and require long reaction times in the order of days.[27,28] Furthermore, the precursors are relatively benign (oxalic acid is commonly used to remove rust) in comparison to these other methods (which often require chemicals with significant hazards such as hydrazine).

The undoped VO_2 sample showed high crystallinity with relatively narrow peak broadening, as estimated from the FWHM values (Table 1a). In comparison with the literature pattern, a preferential orientation along the (2 2 0) plane could be observed for our samples, which is indicated by an increase in the intensity of the (2 2 0) peak compared with the (0 1 1) and
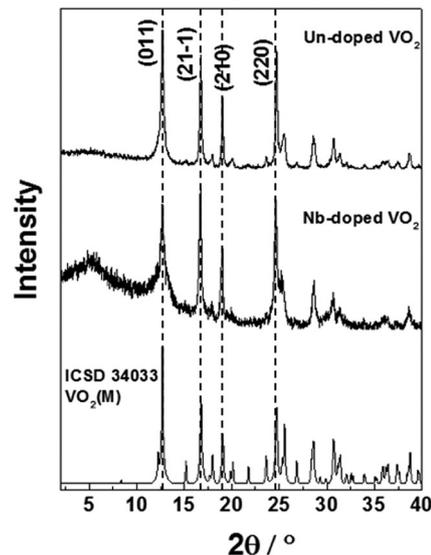

Fig. 2 XRD patterns of the VO_2(M) and Nb-VO_2(M) nanoparticles synthesised by CHFS. The standard XRD pattern of monoclinic VO_2 (ICSD 34033) has been included for reference.

Table 1 Crystal lattice parameters for undoped VO_2(M) and Nb-VO_2(M) at room temperature

| Samples | Crystal lattice parameters (Å) | | | Angle (°) | Cell volume V |
	a	b	c	β	
VO_2(M)	9.133(1)	5.674(1)	4.495(1)	90.69(2)	232.92(6)
Nb-VO_2(M)	9.088(2)	5.784(1)	4.514(1)	91.47(1)	237.3(1)

(2 1 $\bar{1}$) peaks. Peak broadening is slightly higher in the case of the Nb-doped VO_2 sample. This suggests the Nb dopant caused the reduced crystallinity, as the particle sizes of both samples were similar and therefore broadening due to the particle size effects should be approximately equal. We observe a slight change in the relative intensities of the diffraction peaks upon incorporation of the Nb dopant, which could be due to changes in the degree of preferred orientation of the Nb doped samples, or difference in the electron density between Nb^{5+} and V^{4+}. The crystal lattice parameters and the monoclinic angles of the VO_2 and Nb-VO_2 samples, as estimated from the refinement of the XRD patterns, are summarized in Table 1. They correspond to the monoclinic M2 phase, where VO_2 crystallizes in a centered monoclinic system with the space group $C2/m$.[29] VO_2 with the M2 phase has been previously reported in the literature for doped VO_2 systems and VO_2 materials obtained from stress-induced processes.[29,30] This phase has attracted interest in Mott transition studies.

SEM analysis (Fig. 3) showed round-shaped particles for both VO_2 and Nb-VO_2 samples. This morphology differs from the VO_2 nanoparticles previously synthesised by CHFS, which showed rod-like particles.[18] This could suggest that the higher reaction temperature used in this study (402 °C) promoted rapid nucleation that resulted in the rounded nanoparticles. It can also be pointed out that the high uniformity of the sample indicated the ability of the CHFS process to produce consistent quality nanoparticles in a short time.
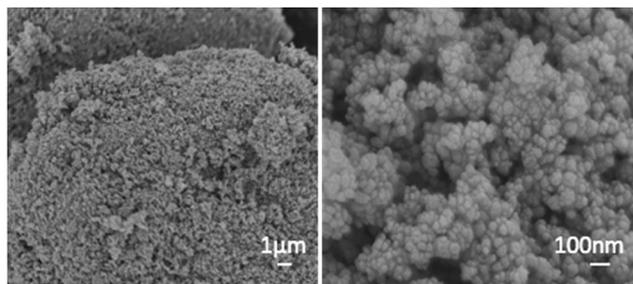
Fig. 3 SEM images of the un-doped VO₂(M) powder.

TEM analysis of the undoped VO₂ and Nb-doped VO₂ samples revealed both samples were formed of a mixture of spherical particles and hexagonal particles (Fig. 4a and b). The particle size analysis of the VO₂(M) and Nb-VO₂(M) samples (50 particles per study) revealed average particle sizes of 33 ± 13 nm and 39 ± 13 nm, respectively (Fig. S2, ESI†). The small particle sizes observed in general were likely due to the high Reynolds number (*i.e.* more turbulent, rapid mixing) for both samples. The smaller particle sizes achieved herein compare extremely favourably with those made previously *via* CHFS, where the particle sizes were in the range of 50–200 nm and particle sizes below 50 nm were only achieved upon significant Nb dopant inclusion. Moreover, the post-synthesis heat-treatment required in the previous study could significantly increase the particle sizes and cause the risk of oxidation. Herein, the direct synthesis of monoclinic VO₂ nanoparticles with smaller particle sizes makes this ideal for thermochromic solar control coatings. Lattice fringes, which could be assigned to the VO₂(M) lattice spacings, were observed in both cases (Fig. 4c and d). In addition, an organic surface coating could be observed on

Fig. 4 TEM images of (a) undoped VO₂ and (b) Nb-doped VO₂. Lattice fringes of (c) undoped VO₂ and (d) Nb-doped VO₂.

some particles (Fig. 4a), which visibly degraded in the beam. It is suggested that surplus oxalic acid is present in the synthesis bound to the surface of the VO₂ particles.

The oxidation states of vanadium and niobium were determined by X-ray photoelectron spectroscopy (XPS). The V $2p_{3/2}$ core-level peak of the undoped sample could be modelled and fitted with two environments, as shown in Fig. 5. It showed the presence of two oxidation states of vanadium, V^{4+} and V^{5+}, at binding energies of 514.8 eV and 516.3 eV, respectively. This indicated that the VO₂ powder is partially oxidized to V₂O₅ at the extreme surface. This is due to the powder being stored in air at room temperature and forming a V₂O₅ passivation layer. The same observation applied to the Nb-doped powder sample. The XPS spectra are shown in Fig. 5. The atomic percentage of the Nb dopant in the doped sample was estimated to be <1 at% by modelling the Nb $3d_{5/2}$ core-level peak. The Nb $3d_{5/2}$ core-level peak is observed at a binding energy of 207.0 eV, which corresponds to the oxidation state of the Nb^{5+} ion. The low intensity of the Nb 3d signal makes definitive chemical identification impossible, so it cannot be ruled out that other chemical environments of Nb are present. Nb doping did not have any significant effect on the oxidation of the VO₂ powder as both samples have been shown to have the same $V^{4+}:V^{5+}$ ratio (*ca.* 33 : 67). This is in contrast to the previous study, where significant changes in the $V^{4+}:V^{5+}$ ratios were observed upon Nb incorporation – resulting in an increase of V^{4+} ions in the doped sample.[19] All the above binding energies are in agreement with literature values (± 0.2 eV).[31,32]

The low levels of Nb detected make the influence of the dopant on the samples questionable. The low atomic percentage could be due to the precursor solution used during the synthesis. Piccirillo *et al.*[33] showed that in the synthesis of Nb-VO₂ films by chemical vapour deposition methods, a Nb/V molar ratio threshold of *ca.* 7.5% was found in order to detect Nb incorporation into the films. This had also been observed with APCVD processes.[34] In the current study, the precursor solution contained a Nb/V molar ratio of 1.25% and this could explain the low dopant level in the powder. In addition, no changes in the $V^{4+}:V^{5+}$ ratio and the particle sizes were observed between the undoped and Nb-doped samples unlike the previous study – suggesting that there is only a small amount of Nb incorporated.[19] Nevertheless, the XRD patterns showed some evidence of substitution of the V^{4+} atoms by the Nb^{5+} atoms.

X-ray absorption spectroscopy

V K-edge X-ray absorption near-edge structure (XANES) spectra for these samples are shown in Fig. 6. The samples are all close in appearance to the monoclinic VO₂ standard, confirming that they are phase-pure.

V K-edge extended X-ray absorption fine structure (EXAFS)/Fourier transforms and best fits are shown in Fig. 7. These data were fitted to a theoretical structure based on ICSD 34033;[35] the fitting model used was similar to that reported by Marini *et al.*[36] The best fit parameters from these fits are given in Table 2. It should be noted that different *k*-space windows were used for the Fourier transforms for the different samples – this is
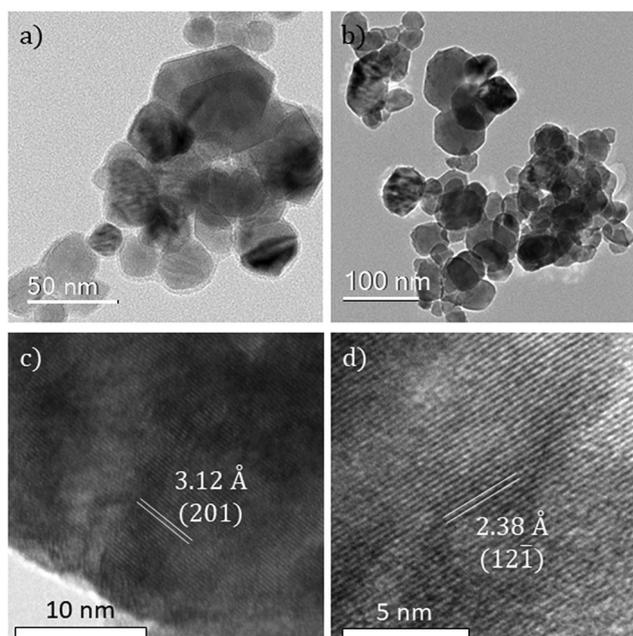
This journal is © The Royal Society of Chemistry 2018

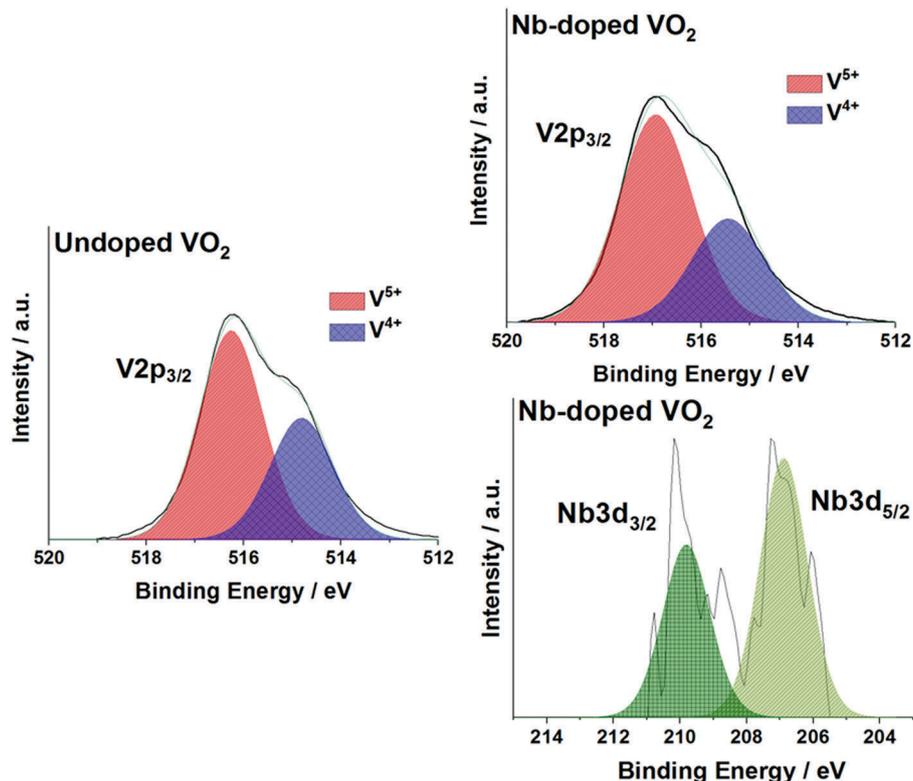*J. Mater. Chem. C*, 2018, **6**, 11731–11739 | 11735

Fig. 5 X-ray photoelectron spectra (XPS) of the V $2p_{3/2}$ and Nb $3d_{5/2}$ environments in the (a) undoped VO_2 and (b) Nb-VO_2 samples.
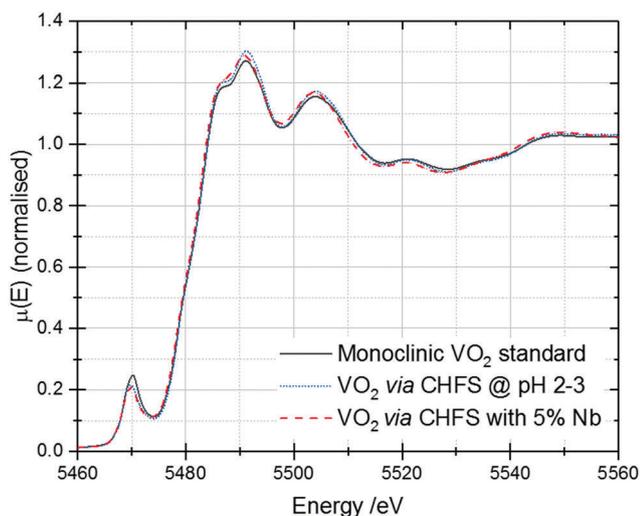

Fig. 6 V K-edge XANES of the VO_2 and Nb-VO_2 samples synthesised by CHFS. A spectrum of a commercial monoclinic VO_2 standard has been included for reference.

however, the two longest V–O distances showed a degree of expansion (without Nb: 2.37 ± 0.04 Å, 2.42 ± 0.04 Å; with Nb: 2.41 ± 0.077 Å, 2.46 ± 0.07 Å; literature: 2.02 Å, 2.06 Å), while all the other distances were (within uncertainty) in line with the literature structure. An increase in (some of) the V–O distances while the V–V distances remain constant suggests that there is an out-of-plane displacement of the oxygen ions, as indicated by the purple arrows in Fig. 8.

The longer V–O paths, which show the greatest expansion, also show increased Debye–Waller factors, indicating increased disorder in these paths. The increased disorder in the out-of-plane direction indicated in Fig. 8 would explain both the increased Debye–Waller factors and the increased average path length in this direction.

The Nb-doped sample showed a slight increase in the average distance for these V–O bonds. This suggests that the substitution of Nb^{5+} into the vanadium dioxide lattice slightly increases this disorder, although this cannot be established with certainty due to the uncertainties on the fitted parameters.

Thus, the EXAFS data confirmed the monoclinic structure of these vanadium dioxide samples and confirmed that this structure is maintained after Nb doping. It also identified out-of-plane disorder of some of the oxygen atoms.

Thermochromic properties

The optical properties of the $VO_2(M)$ nanoparticles were measured by recording their transmittance spectra from 250 nm to 2500 nm up to 90 °C (Fig. 9). All samples displayed thermochromic

responsible for the differences in the appearance of the samples in Fig. 7a. This was done to include the maximum possible data range in the fit, while excluding noise/high-k artefacts – this enables fitting of the highest possible number of parameters to the best precision.

The EXAFS of each of the samples were broadly consistent with the literature structure of monoclinic vanadium dioxide;
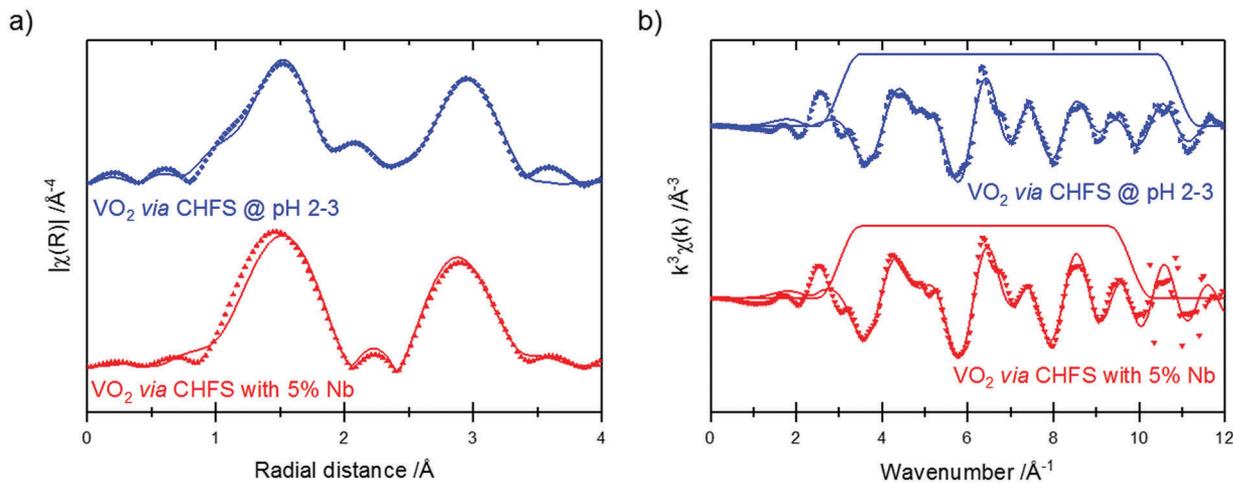
Fig. 7 V K-edge Fourier transforms (a) and EXAFS (b) of the CHFS VO$_2$ samples. Data are plotted as symbols, and fits as solid lines. The trapezoid lines in (b) indicate the Fourier transform window used.

Table 2 EXAFS best fit parameters for the VO$_2$ samples prepared via CHFS. R is the half path length, σ^2 is the EXAFS Debye−Waller factor and R-factor is the crystallographic R-factor. All values are rounded as appropriate for their uncertainties, and uncertainties in the final digits are given in parentheses after the values. Path lengths indexed as $\delta,\varepsilon,\zeta,\theta,\iota$ or κ were refined with a common refinement parameter across all paths with the same index. Debye−Waller factors indexed as η,μ or λ were constrained to be the same across all paths with the same index

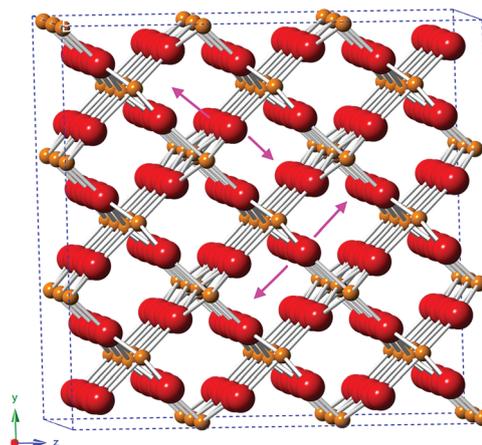| Sample	Path	Degeneracy	$R/\text{Å}$	$\sigma^2/\text{Å}^{-2}$	R factor
VO$_2$ via CHFS	V–O	1	1.83(5)	0.009(5)	0.008
		2	1.96(2)		
		2	2.37(4)$^\delta$	0.016(9)$^\eta$	
		1	2.42(4)$^\delta$		
	V–V	1	2.61(3)	0.008(4)	
		1	3.17(9)		
		2	3.41(9)$^\varepsilon$		
		2	3.49(9)$^\varepsilon$		
		2	3.4(2)$^\zeta$	0.016(9)$^\eta$	
		2	3.5(2)$^\zeta$		
Nb-VO$_2$ via CHFS	V–O	1	1.85(1)$^\theta$	0.0025(9)$^\lambda$	0.010
		2	1.97(1)$^\theta$		
		2	2.41(7)$^\iota$	0.013(4)	
		1	2.46(7)$^\iota$		
	V–V	1	2.7(2)	0.02(1)$^\mu$	
		1	3.3(4)		
		2	3.42(2)$^\kappa$	0.0025(9)$^\lambda$	
		2	3.50(2)$^\kappa$		
		2	3.59(2)$^\kappa$	0.013(4)$^\mu$	
		2	3.66(2)$^\kappa$		

Fig. 8 Structure of monoclinic VO$_2$, based on ICSD 34033, indicating the direction of the proposed out-of-plane oxygen displacement (purple arrows). O^{2-}: red; V^{4+}: orange.

behaviour with a reversible switch around *ca.* 68 °C – corresponding to the typical transition temperature expected for undoped VO$_2$. The luminous and solar transmittance (T_{lum} and T_{sol}) were estimated based on the measured spectra using the equation below (Table 3):

$$T_{\text{lum,sol}}^{\sigma} \equiv \frac{\int \Phi_{\text{lum,sol}} T^{\sigma}(\lambda)\text{d}\lambda}{\int \Phi_{\text{lum,sol}}(\lambda)\text{d}\lambda} \qquad (1)$$

where λ is the wavelength of light, ϕ_{lum} is the solar irradiance weighted to the sensitivity of the human eye, ϕ_{sol} is the weighted solar irradiance spectrum, and T^{σ} is the transmission

of the VO$_2$ thin film in either the hot state or the cold state. From the above equation, the solar modulation (ΔT_{sol}) can be deduced from the difference between the solar transmittance in the cold and hot states:

$$\Delta T_{\text{sol}} = T_{\text{sol}} (25\ °\text{C}) - T_{\text{sol}} (90\ °\text{C}) \qquad (2)$$

The modulation in the infrared region (ΔT_{IR}) was also estimated from eqn (2) as it only takes into account the near-infrared region (750 to 2500 nm) of the measured spectra, which is specific for the thermochromic functionality expected.

The undoped VO$_2$ powder showed a ΔT_{sol} of 3.8%, which is in line with those of the un-doped VO$_2$ materials synthesised by other methods such as magnetron sputtering or APCVD.[37–39] The powder exhibited a good efficiency for modulating infrared radiation with a ΔT_{IR} of 7%, however, it displayed a low visible light transmittance (T_{lum} = 14%).

Several studies showed that doping VO$_2$ samples with niobium is usually accompanied by a decrease of the visible
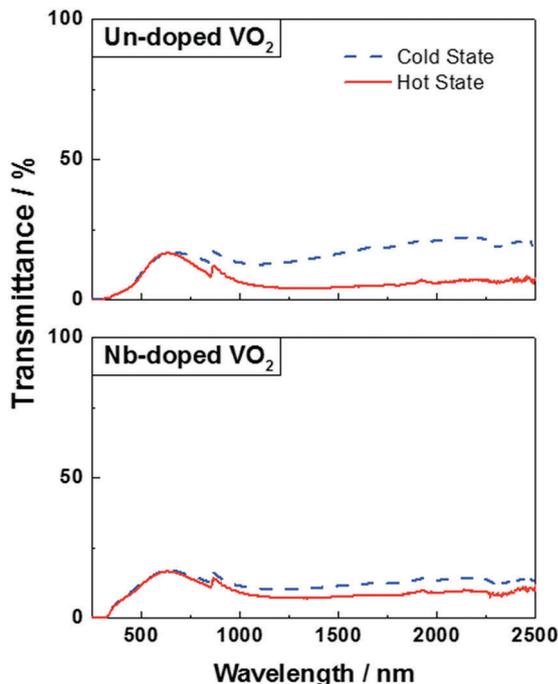
This journal is © The Royal Society of Chemistry 2018

J. Mater. Chem. C, 2018, **6**, 11731–11739 | **11737**

Fig. 9 UV-Vis spectra of un-doped VO_2 (top) and Nb-doped VO_2 (bottom) at 20 °C (blue dashed line) and 90 °C (continuous red line).

Table 3 Visible light transmittance T_{lum} in the cold and hot states, solar modulation ΔT_{sol} and solar modulation in the NIR region ΔT_{IR} for the un-doped VO_2 and Nb-doped VO_2 samples

Samples	T_{lum} (%)		ΔT_{sol} (%)	ΔT_{IR} (%)
	Cold state	Hot state		
Un-doped VO_2	14	14	3.8	7
Nb-doped VO_2	15	15	1.5	2.4

light transmittance T_{lum} and a MST reduction.[40–42] Both samples, however, have a similar T_{lum} of 15% and 14% for the doped and un-doped samples, respectively. Moreover, the transition temperature (MST) of the doped sample is around *ca.* 68 °C, which is the MST observed for a typical undoped VO_2 material. This can be explained by the very low at% of niobium present in the powder – the atomic percentage is too low for observing any effect on the optical properties. On the other hand, Table 3 shows a poor ability of the Nb-doped sample to modulate infrared radiation, which can be seen by a drop in the ΔT_{sol} (1.5%) and ΔT_{IR} (2.4%) when compared to the undoped powder. This is most likely due to the lower crystallinity of the doped material. It has been shown that a poor crystallinity of the VO_2 samples resulted in a low solar modulation.[39] Furthermore, both samples have been shown to have the same $V^{4+}:V^{5+}$ ratio and similar average particle sizes.

As a result, the undoped VO_2 nanoparticles synthesised by CHFS showed good thermochromic properties. Both samples have been revealed to have a low luminous transmittance, which could be caused by the sample preparation for UV-Vis measurements. The small average particle sizes of the samples

suggest that a good dispersion of the NPs in a host could significantly increase the T_{lum}. Doping with niobium did not seem to have any impact on the luminous transmittance and the MST. Only a change in the ΔT_{sol} has been observed and is most likely a result of the differing degrees of crystallinity.

Conclusions

Pure monoclinic VO_2 nanoparticles (undoped and doped with niobium) were successfully synthesised by CHFS at a mixer reaction temperature of *ca.* 400 °C. The synthesis was direct and no post-synthesis heat-treatment of the samples was required. The vanadium(IV) precursor solution was immediately converted into a VO_2(M) nanoparticle slurry in the process. The undoped VO_2 powder possessed good thermochromic properties, a ΔT_{sol} of 3.8% and a ΔT_{IR} of 7%, but a low visible light transmittance, which could be attributed to the sample preparation. The Nb-doped sample was synthesised using a Nb/V solution with a molar ratio of 1.25%. The XRD patterns and XANES and EXAFS analyses highlighted some evidence of Nb^{5+} substitutions into the VO_2 lattice, suggesting that the Nb dopant induced a relatively poor VO_2 crystallinity. Nevertheless, the molar ratio of the Nb/V solution was too low to have any significant effect on the MST and the optical properties of the sample, or for definitive conclusions on the nature of the Nb in the sample to be ascertained. Despite the low luminous transmittance for both samples, the TEM images showed small particle sizes (in the range of 30 to 40 nm), which could lead to a significant increase of the T_{lum} if the particles are well dispersed in a host in the future.

Conflicts of interest

There are no conflicts to declare.

Acknowledgements

References

1 M. Lübke, N. Ding, M. J. Powell, D. J. L. Brett, P. R. Shearing, Z. Liu and J. A. Darr, *Electrochem. Commun.*, 2016, **64**, 56–60.
2 L. Jiang, Y. Qu, Z. Ren, P. Yu, D. Zhao, W. Zhou, L. Wang and H. Fu, *ACS Appl. Mater. Interfaces*, 2015, **7**, 1595–1601.
3 Y. Qin, G. Fan, K. Liu and M. Hu, *Sens. Actuators, B*, 2014, **190**, 141–148.
4 J. Zhou, Y. Gao, Z. Zhang, H. Luo, C. Cao, Z. Chen, L. Dai and X. Liu, *Sci. Rep.*, 2013, **24**, 1–5.

11738 | *J. Mater. Chem. C*, 2018, **6**, 11731–11739

This journal is © The Royal Society of Chemistry 2018

5 G. Sun, X. Cao, X. Gao, S. Long, M. Liang and P. Jin, *Appl. Phys. Lett.*, 2016, **109**, 143903.

6 Z. Zhang, Y. Gao, Z. Chen, J. Du, C. Cao, L. Kang and H. Luo, *Langmuir*, 2010, **26**, 10738–10744.

7 C. G. Granqvist, S. Green, G. A. Niklasson, N. R. Mlyuka, S. von Kræmer and P. Georén, *Thin Solid Films*, 2010, **518**, 3046–3053.

8 D. Vernardou, M. E. Pemble and D. W. Sheel, *Chem. Vap. Deposition*, 2006, **12**, 263–274.

9 S. Y. Li, G. A. Niklasson and C. G. Granqvist, *J. Appl. Phys.*, 2011, **109**, 1–6.

10 S. Y. Li, G. A. Niklasson and C. G. Granqvist, *J. Appl. Phys.*, 2010, **108**, 63525.

11 C. G. Granqvist, *Mater Today: Proc.*, 2016, **3**, S2–S11.

12 K. Laaksonen, S. Y. Li, S. R. Puisto, N. K. J. Rostedt, T. Ala-Nissila, C. G. Granqvist, R. M. Nieminen and G. A. Niklasson, *Sol. Energy Mater. Sol. Cells*, 2014, **130**, 132–137.

13 N. Wang, Q. Sheng, P. Lin, S. Magdassi and Y. Long, *J. Alloys Compd.*, 2017, **711**, 222–228.

14 J. Zhu, A. Huang, K. Tong, S. Ji, S. Bao, X. Cao and P. Jin, *ACS Appl. Mater. Interfaces*, 2016, **8**, 29742–29748.

15 J. A. Darr, J. Zhang, N. M. Makwana and X. Weng, *Chem. Rev.*, 2017, **117**, 11125–11238.

16 M. Lübke, I. Johnson, N. M. Makwana, D. Brett, P. Shearing, Z. Liu and J. A. Darr, *J. Power Sources*, 2015, **294**, 94–102.

17 T. Adschiri, K. Kanazawa and K. Arai, *J. Am. Ceram. Soc.*, 1992, **22**, 1019–1022.

18 M. J. Powell, P. Marchand, C. J. Denis, J. C. Bear, J. A. Darr and I. P. Parkin, *Nanoscale*, 2015, **7**, 18686–18693.

19 R. Quesada-Cabrera, M. J. Powell, P. Marchand, C. J. Denis, J. A. Maggio, F. Di Darr and I. P. Parkin, *J. Nanosci. Nanotechnol.*, 2016, **16**, 10104–10111.

20 R. I. Gruar, C. J. Tighe and J. A. Darr, *Ind. Eng. Chem. Res.*, 2013, **52**, 5270–5281.

21 I. D. Johnson, M. Loveridge, R. Bhagat and J. A. Darr, *ACS Comb. Sci.*, 2016, **18**, 665–672.

22 A. J. Dent, G. Cibin, S. Ramos, A. D. Smith, S. M. Scott, L. Varandas, R. M. Pearson, N. A. Krumpa, C. P. Jones and P. E. Robbins, *J. Phys. Conf. Ser.*, 2009, **190**, 12039.

23 B. Ravel and M. Newville, *J. Synchrotron Radiat.*, 2005, **12**, 537–541.

24 D. N. Sathyanarayana and C. C. Patel, *J. Inorg. Nucl. Chem.*, 1965, **27**, 297–302.

25 D. N. Sathyanarayana and C. C. Patel, *J. Inorg. Nucl. Chem.*, 1966, **28**, 2277–2283.

26 T. G. Ros, M. K. Van Der Lee, A. J. Van Dillen, J. W. Geus and D. C. Koningsberger, *J. Mol. Catal. A: Chem.*, 2002, **186**, 13–24.

27 J. H. Son, J. Wei, D. Cobden, G. Cao and Y. Xia, *Chem. Mater.*, 2010, **22**, 3043–3050.

28 J. Zhou, Y. Gao, X. Liu, Z. Chen, L. Dai, C. Cao, H. Luo, M. Kanahira, C. Sun and L. Yan, *Phys. Chem. Chem. Phys.*, 2013, **15**, 7505.

29 M. Marezio, D. B. McWhan, J. P. Remeika and P. D. Dernier, *Phys. Rev. B: Solid State*, 1972, **5**, 2541–2551.

30 K. Okimura, T. Watanabe and J. Sakai, *J. Appl. Phys.*, 2012, **111**, 1–7.

31 G. Silversmit, D. Depla, H. Poelman, G. B. Marin and R. De Gryse, *J. Electron Spectrosc. Relat. Phenom.*, 2004, **135**, 167–175.

32 P. E. Sobol and J. Chastain, *Handbook of X-ray Photoelectron Spectroscopy*, 1993.

33 C. Piccirillo, R. Binions and I. P. Parkin, *Eur. J. Inorg. Chem.*, 2007, 4050–4055.

34 T. D. Manning, I. P. Parkin, M. E. Pemble, D. Sheel and D. Vernardou, *Chem. Mater.*, 2004, **16**, 744–749.

35 J. M. Longo and P. Kierkegaard, *Acta Chem. Scand.*, 1970, **24**, 420–426.

36 C. Marini, S. Pascarelli, O. Mathon, B. Joseph, L. Malavasi and P. Postorino, *EPL*, 2013, **102**, 66004.

37 N. R. Mlyuka, G. A. Niklasson and C. G. Granqvist, *Sol. Energy Mater. Sol. Cells*, 2009, **93**, 1685–1687.

38 M. J. Powell, R. Quesada-Cabrera, A. Taylor, D. Teixeira, I. Papakonstantinou, R. G. Palgrave, G. Sankar and I. P. Parkin, *Chem. Mater.*, 2016, **28**, 1369–1376.

39 D. Malarde, M. J. Powell, R. Quesada-cabrera, R. L. Wilson, C. J. Carmalt, G. Sankar, I. P. Parkin and R. G. Palgrave, *ACS Omega*, 2017, **2**, 1040–1046.

40 Y. Li, Y. Liu, J. Liu and L. Ren, *J. Mater. Sci.: Mater. Electron.*, 2016, **27**, 4981–4987.

41 H. M. Pinto, J. Correia, R. Binions, C. Piccirillo, I. P. Parkin and V. Teixeira, *Mater. Sci. Forum*, 2008, **587**, 640–644.

42 C. Batista, J. Carneiro, R. M. Ribeiro and V. Teixeira, *J. Nanosci. Nanotechnol.*, 2011, **11**, 9042–9045.